DOI: 10.1002/anie.201204675

Water Splitting

Freestanding Tin Disulfide Single-Layers Realizing Efficient Visible-Light Water Splitting**

Yongfu Sun, Hao Cheng, Shan Gao, Zhihu Sun, Qinghua Liu, Qin Liu, Fengcai Lei, Tao Yao, Jingfu He, Shiqiang Wei, and Yi Xie**

Natural photosynthesis shows the direct conversion of solar energy into chemical fuels. However, even the green plants, after aeons of evolution, only perform this task with an efficiency of a few percent,[1] which restricts the global potential of using direct bioenergy conversion as a fuel source on a large scale. Therefore, bioinspired artificial photosynthetic strategies are attracting tremendous interest, with a view to mimicking the natural photoconversion of sunlight to useful fuels in a more efficient way. In this regard, photoelectrochemical (PEC) cells, which can mimic the photosynthetic process within a leaf by splitting water to produce H_2 and O_2, have recently emerged as the most prominent systems.[2–5] In addition to possessing a free and unlimited supply of solar energy and water, the fascination also comes from their environmentally benign reactions under nearly neutral conditions without generating polluted byproducts such as carbon dioxide. Despite these excellent advantages, the practical applications are still handicapped by their low efficiency and poor stability. Thus, further breakthroughs in the design and synthesis of novel photoelectrode materials, with a high conversion efficiency and stable cycling behavior, hold the key to the development of PEC water splitting.

The factors limiting the efficiency of solar water splitting mainly concentrate on the following aspects: 1) most of the photocatalysts solely absorb UV light, which accounts for only 4% of the total sunlight; 2) they usually suffer from sluggish charge transfer and water oxidation kinetics.[6,7] To better use the solar light for energy conversion, the development of visible-light-responsive photocatalysts is highly desirable because visible light contributes to the solar spectrum with about 43%. As such, inorganic graphene analogs (IGAs) with a visible-light band gap may represent ideal architectures for high-performance PEC electrodes. These IGAs provide a type of architecture that could offer a huge specific surface area and large fraction of uncoordinated surface atoms for harvesting more visible light, while photon absorption in bulk or nanosized particles is often limited by light transmittance and reflection at the grain boundaries.[8,9] Also, according to the diffusion formula of $t = d^2/k^2D$ (d is the particle size, k is a constant, D is the diffusion coefficient of electron–hole pairs),[10] the atomically ultrathin thickness and two-dimensional (2D) conducting channels help them to achieve rapid carrier transport in photoelectrodes with a greatly reduced recombination rate.[10–12] Moreover, the 2D configuration with huge surface area allows for intimate contact with the substrate and high interfacial contact area with the electrolyte, thus facilitating fast interfacial charge transfer and electrochemical reactions as well as low corrosion rates.[13]

Inspired by the aforementioned concepts, it is highly desirable to explore the synthesis of visible-light-responsive IGAs in efforts to achieve efficient PEC water splitting. Generally speaking, controllable exfoliation of layered compounds is regarded as the exclusive way to obtain graphene-like single layers. In this case, the structural analysis shows that hexagonal tin disulfide would be an appealing bridge for fabricating visible-light-responsive IGAs. In addition to being nontoxic, low-priced, and chemically stable in acidic or neutral aqueous solutions hexagonal SnS_2 possesses a visible-light band gap of 2.2–2.35 eV and a peculiar CdI_2-type layered structure consisting of a S-Sn-S triple layer, in which the layers are held together by Van der Waals interactions (see Scheme S1 in the Supporting Information).[14,15] For this reason, it is really indispensable and challenging to develop a synthetic route for the fabrication of SnS_2 single-layers, which offer the possibility for manipulating visible-light water splitting.

Herein, we put forward a scalable exfoliation strategy to accomplish this challenge by refluxing bulk SnS_2 in formamide (Figure 1A), giving the first synthetic case for freestanding SnS_2 single-layers with three atom thickness. As shown by the X-ray diffraction pattern (XRD) in Figure 1C, the sole strong diffraction peak for the exfoliated products could be readily assigned to the (002) facet of hexagonal SnS_2 (P63 mc, joint committee on powder diffraction standards, JCPDS, card number 89-3198), while other small diffraction peaks could also be indexed to their (004) and (006) facets.

[*] Dr. Y. F. Sun, S. Gao, F. C. Lei, Prof. Y. Xie
Hefei National Laboratory for Physical Sciences at Microscale
University of Science & Technology of China
Hefei, Anhui 230026 (P.R. China)
E-mail: yxie@ustc.edu.cn
H. Cheng, Dr. Z. H. Sun, Dr. Q. H. Liu, Q. Liu, Dr. T. Yao, Dr. J. F. He, Prof. S. Q. Wei
National Synchrotron Radiation Laboratory
University of Science & Technology of China
Hefei, Anhui 230029 (P.R. China)
E-mail: sqwei@ustc.edu.cn

[**] This work was financially supported by the National Basic Research Program of China (grant number 2009CB939901) and the National Nature Science Foundation (grant numbers 11079004, 10979047, 90922016, and 11135008).

Supporting information for this article, including experimental details, calculation details, results, structural models, XPS and Raman spectra, Mott–Schottky plots, *I–t* curves and EXAFS curve-fitting results, is available on the WWW under http://dx.doi.org/10.1002/anie.201204675.

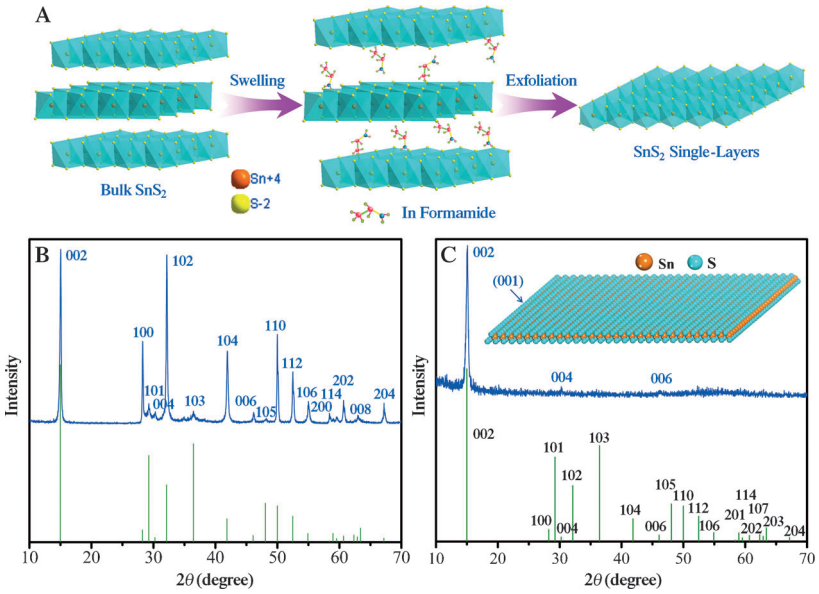

Figure 1. A) Exfoliation of hexagonal layered SnS_2 into (001)-oriented freestanding SnS_2 single-layers. XRD patterns for B) bulk SnS_2 and C) (001)-oriented freestanding SnS_2 single-layers.

This reasonably indicates that the (001) orientation is highly preferred, which is further verified by the corresponding high-resolution transmission electron microscopy (TEM) image and the selected-area electron diffraction patterns in Figure 2C,D. Also, the X-ray photoelectron spectra in Figure S1 A–C in the Supporting Information further confirm the formation of pure hexagonal SnS_2.[16,17] Meanwhile, Raman spectra shown in Figure S1 D provide additional insights into the chemical composition of the products. As for the exfoliated SnS_2, the Raman bands at 310.4 and 200 cm^{-1} correspond to the A_{1g} and E_g mode of hexagonal SnS_2, respectively. Obviously, compared to the bulk material, the Raman bands of the exfoliated SnS_2 shift towards lower wavenumbers. This behavior could be ascribed to the phonon confinement effect and reasonably infer the ultrathin thickness of the SnS_2 single-layers.[16–19]

Moreover, Figures 1B and 2A display the XRD pattern and scanning electron microscopy (SEM) image of bulk hexagonal SnS_2, showing a typical plate-like morphology with lateral size of about 3 μm and a thickness of about 100 nm. In contrast, the TEM image of the exfoliated products displayed in Figure 2B clearly shows a large-area 2D sheet-like structure with a size larger than 500 nm, while the nearly transparent feature indicates the ultrathin thickness, which is further verified by the atomic force microscopic (AFM) image and the corresponding height profile shown in Figure 2E,F. Meanwhile, the colloidal dispersions of the exfoliated products are highly stable over a period of several days and display a typical Tyndall effect, reasonably indicating the formation of freestanding and homogeneous 2D ultrathin sheets (inset in Figure 2B). Furthermore, as depicted in Figure 2E,F, the AFM image and the corresponding height profile display the smooth and large sheet-like morphology with a height of about 6.1 Å, which agrees well with the 5.91 Å of a single-layered SnS_2 slab along the [001] direction (Scheme S1 in the Supporting Information), providing direct and solid evidence for the formation of large-area SnS_2 single-layers with three atom thickness. More importantly, this method is simple and can be easily scaled up since the yield is limited exclusively by the size of the flask. Therefore, all the above-mentioned results unambiguously show the large-scale exfoliation of bulk SnS_2 into large-area SnS_2 freestanding single-layers, thus providing the prerequisites for their application in the construction of large-area nanodevices.

To study the visible-light water-splitting properties of the SnS_2 single-layers, a photoelectrode was prepared by spin-coating ethanol dispersions of the SnS_2 single-layers on indium-tin-oxide (ITO) coated glass. The PEC water splitting was investigated by PEC measurements in a 0.5 M Na_2SO_4 electrolyte using a three-electrode setup. In effect, as depicted in Figure 3A, the dark currents of

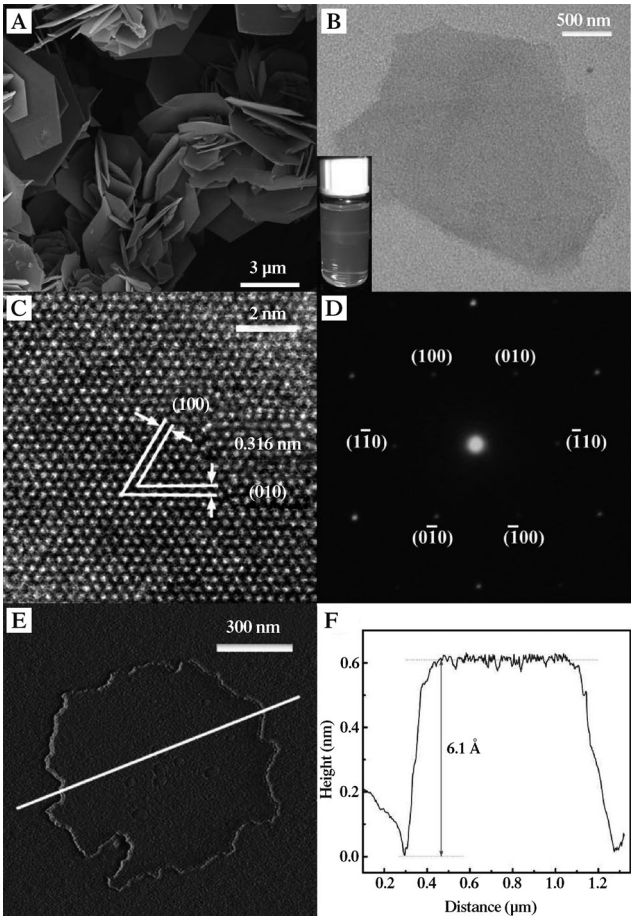

Figure 2. A) SEM image for bulk hexagonal SnS_2. Characterizations for (001)-oriented freestanding SnS_2 single-layers. B) TEM image and the corresponding colloidal ethanol/water (1:1) dispersion displaying the Tyndall effect. C) HRTEM and D) the corresponding selected-area electron diffraction. E) AFM image and F) the corresponding height profile.

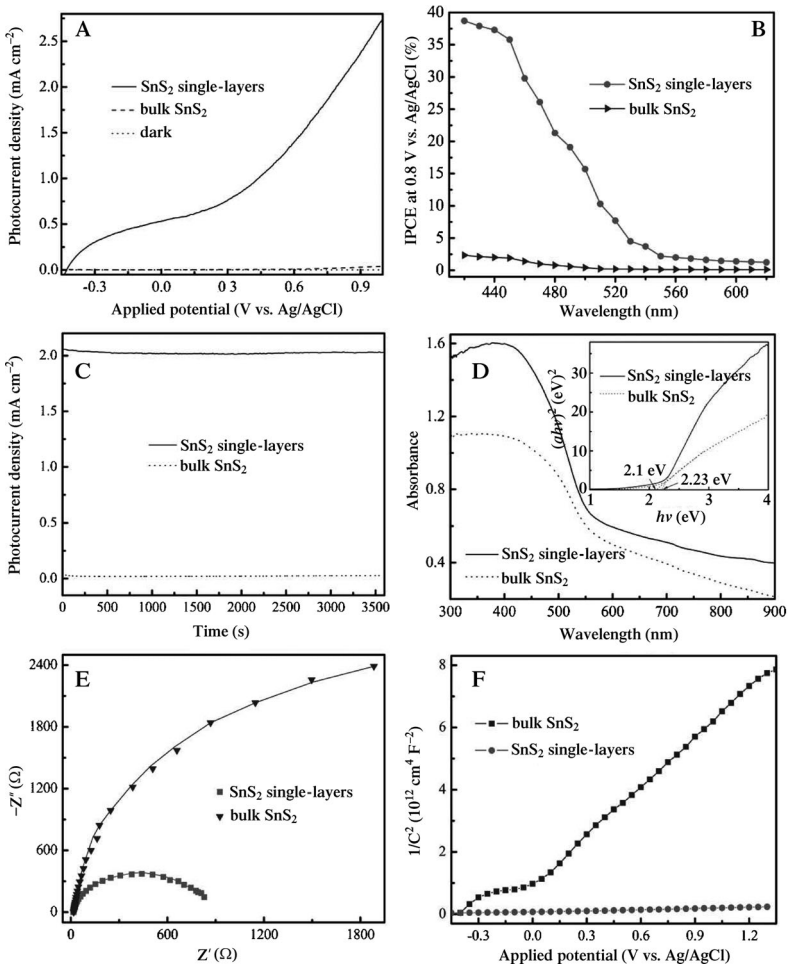

Figure 3. A) Photocurrent curves at 300 W Xe lamp irradiation ($\lambda > 420$ nm). B) Incident photon-to-current conversion efficiency. C) *I*–*t* curves at 0.8 V versus Ag/AgCl at irradiation by a 300 W Xe lamp ($\lambda > 420$ nm; I = photocurrent density and t = time). D) UV/Vis diffuse reflectance spectra (α, h, and ν are the absorption coefficient, Planck's constant, and light frequency). E) Electrochemical impedance spectra. Z' and Z'' are the real and imaginary parts of the impedance, while the solid lines were fitted by ZSimpWin software using the equivalent circuits. F) Mott–Schottky plots.

SnS_2 single-layers and the bulk material remained at a level of less than 5 $\mu A\,cm^{-2}$ at the applied potentials between −0.45 and 1.0 V versus Ag/AgCl. Contrastingly, at visible-light irradiation of 300 W from a Xe lamp, the SnS_2 single-layers displayed a much enhanced photocurrent density of 2.75 $mA\,cm^{-2}$ at 1.0 V, roughly 72 times larger than that of the bulk material (Figure 3A). Measurement of the incident photon-to-current conversion efficiency (IPCE) is a powerful tool for probing the photoconversion efficiency of different photoelectrodes because this method is independent in the light source and filters used for the measurements.[20] The IPCE can be expressed concretely as given in Equation (1),

$$\mathrm{IPCE} = \frac{hcI}{\lambda J_{\mathrm{light}}}$$

where h is the Planck constant, c is the speed of light, I is the measured photocurrent density at a specific wavelength, λ is the wavelength of the incident light, and J_{light} is the irradiance intensity at a specific wavelength. As depicted in Figure 3B, one can clearly observe that the IPCE onset of the SnS_2 single-layers is located at around 540 nm, which corresponded to a band gap of about 2.29 eV and matches well with the measured absorption edge of 2.23 eV in Figure 3D. Also, Figure 3B shows an IPCE of 38.7% at 420 nm, which is significantly higher than the 2.33% for the bulk material. Actually, the visible-light conversion efficiency of 38.7% is much better than that of most existing reports,[7,21–25] implying an efficient transport and separation of photogenerated carriers in the SnS_2 single-layers. An important finding was that the photocurrent densities of the SnS_2 single-layers showed negligible variation after even 3600 s of irradiation, while the bulk material displayed serious *I*–*t* fluctuations (Figure 3C and Figure S3), clearly revealing the remarkably enhanced photostability of SnS_2 single-layers.

Notably, the greatly improved visible-light water splitting behavior of SnS_2 single-layers could be ascribed to the synergistic effect between their macroscopic morphological features and microscopic atomic/electronic structure. The huge specific surface area and high-percentage of disordered surface atoms enabled them to harvest remarkably increased visible light (Figure 3D).[26] The carriers photogenerated deeply within the semiconductor took a longer time to reach the surface than those generated close to the surface, and so were more likely to be lost on account of recombination before they could be collected.[10–12,27] Thus, the atomically ultrathin thickness of the SnS_2 single-layers contributed to the strikingly fast carrier transport from the inside to the surface. Also, their 2D configuration endowed them with a much better grain boundary connectivity and intimate contact with the ITO substrate, verified by the much lower interfacial charge-transfer resistance in Figure 3E,[11,12,28] which helps to greatly enhance the carrier transport/separation efficiency. To better understand the carrier transport in the electrode of SnS_2 single-layers, electrochemical impedance measurements were performed to determine their capacitance. The carrier density (N_D) and the flat band potential (V_{fb}) can be estimated by the Mott–Schottky Equation (2),[29]

$$C_{sc}^{-2} = \frac{2}{e_0\varepsilon_0\varepsilon_r N_D}\left(V - V_{fb} - \frac{kT}{e_0}\right)$$

where C_{sc} is the capacitance of the space charge layer, e_0 is the electron charge, ε_0 is the vacuum permittivity, ε_r is the dielectric constant, V is the applied potential, T is the absolute temperature, and k is the Boltzmann constant. N_D was calculated using Equation (3).

$$N_D = (2/e_0\varepsilon_0\varepsilon_r)\left[\mathrm{d}\left(1/C^2\right)/\mathrm{d}V\right]^{-1}$$

The positive slopes in Figure 3F and Figure S2 in the Supporting Information showed that both the SnS_2 single-layers and the bulk material were n-type semiconductors. The electron density of SnS_2 single-layers was calculated to be 5.87×10^{19} cm^{-3} ($\varepsilon_r=17.7$),[30] roughly 40 times higher than the 1.48×10^{18} cm^{-3} for the bulk material, thus facilitating the charge transport in SnS_2 single-layers and at the interface between the ITO and the SnS_2 single-layers.[31] Meanwhile, the V_{fb} of the SnS_2 single-layers was determined to be −0.45 V by extrapolation of the X intercepts in Mott–Schottky plots, and the found potential is more cathodic than the potential of −0.23 V for the bulk material. The negative V_{fb} shift could be ascribed to the substantially increased electron density that shifted the Fermi level of the SnS_2 single-layers upward[31] and also reflected the greatly decreased carrier recombination.[32] Moreover, the width of the space charge layer (W) at the interface of the SnS_2 single-layers and the electrolyte can also be quantified by the Equation (4).

$$W=\left[\frac{2\varepsilon_0\varepsilon_r(V-V_{jb})}{e_0N_D}\right]^{\frac{1}{2}}$$

At a potential of 1.0 V versus Ag/AgCl, W was calculated to be about 7 nm, which is remarkably thicker than the height of SnS_2 single-layers, meaning that the SnS_2 single-layers could be fully depleted and hence the photoexcited carriers can be efficiently separated under the applied potentials.[33] Furthermore, as a benefit of the large contact area to the electrolyte, the SnS_2 single-layers allowed surface reactions to take place across a much larger area relative to the bulk material, that is, the reaction space was greatly enlarged.[34]

To give an in-depth understanding of the high IPCE of the SnS_2 single-layers, X-ray absorption fine structure spectroscopy (XAFS) measurements at the Sn K-edge were performed and are displayed in Figure 4A,B. The $k^2\chi(k)$ oscillation curve (k = wave vector and $\chi(k)$ = oscillation as a function of the photoelectron wavenumber) for the SnS_2 single-layers showed a similar spectral shape with regard to the bulk material, albeit a noticeable reduction in oscillation amplitude is observed. The Fourier transformed (FT) $k^2\chi(k)$ functions could more explicitly manifest this amplitude reduction. As depicted in Figure 4B, the FT curve of the bulk SnS_2 material displayed two peaks at 2.09 and 3.37 Å, corresponding to the Sn-S and Sn-Sn correlations. By contrast, the peak intensities of the SnS_2 single-layers dropped significantly and the corresponding peak positions slightly shifted by 0.02 Å in the R direction. To obtain quantitative structural parameters around the Sn atoms in the SnS_2 single-layers and the bulk material, least-square curve parameter fitting of the Sn-S and Sn-Sn peaks was performed, with the results summarized in Table S1 in the Supporting Information. Evidently, compared with the bulk material, the interatomic distances of the Sn-S and Sn-Sn coordinations in the SnS_2 single-layers were relatively elongated, while the degree of disorder was remarkably increased. According to these structural parameters, the structural models for SnS_2 single-layers are displayed in Figure 4C,D, which clearly show the distorted bond lengths and bond angles of Sn-S, Sn-Sn and Sn-S-Sn coordination geometries. This intralayer structural distortion supported the minimization of the surface energy and hence endowed the material with excellent structural stability upon the formation of SnS_2 single-layers. Notably, the surface distortion of SnS_2 single-layers would inevitably influence their electronic properties, which could be further shown by the corresponding first-principles calculations. The calculated densities of states (DOS) in Figure S4 showed that the SnS_2 single-layers possessed an obviously increased density of states at the edge of the valence band relative to the bulk material. The eminently increased DOS contributed to realize higher carrier mobility,[35] thus definitely determining their remarkably enhanced visible-light water-splitting properties.

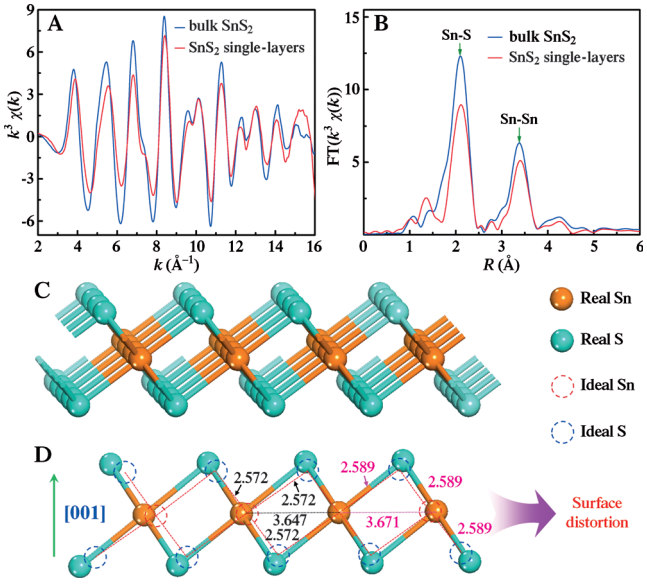

Figure 4. A) Sn K-edge extended XAFS oscillation function $k^3\chi(k)$ and B) the corresponding Fourier transforms FT($k^3\chi(k)$); k = wave vector and $\chi(k)$ = oscillation as a function of the photoelectron wavenumber. C) Three-dimensional and D) two-dimensional structural models for SnS_2 single-layers.

In conclusion, freestanding SnS_2 single-layers with three atom thickness were first synthesized through a convenient and scalable liquid exfoliation strategy, thus offering an excellent platform to achieve efficient visible-light water splitting. Synchrotron radiation XAFS and first-principles calculations disclosed that the surface atomic elongation and structural disorder of the SnS_2 single-layers contributed to the excellent structural stability and increased density of states at the valence band edge. Taking advantage of efficient visible-light harvesting, an improved carrier density, a fully depleted space charge layer, and fast interfacial charge transfer as well as facile electrochemical reactions, the SnS_2 single-layers yield a photocurrent density up to 2.75 mA cm^{-2} at 1.0 V versus Ag/AgCl, which is over 70 times higher than that of the bulk material. Also, the SnS_2 single-layers reached a visible-light conversion efficiency of 38.7% that is superior to most existing reports. This work will have impact on the design of efficient PEC and photovoltaic devices.

Received: June 15, 2012
Published online: July 24, 2012

Keywords: electrochemistry · monolayers · photosynthesis · water splitting

[1] J. Michl, *Nat. Chem.* **2011**, *3*, 268.
[2] A. Fujishima, K. Honda, *Nature* **1972**, *238*, 37.
[3] Z. G. Yi, J. H. Ye, N. Kikugawa, T. Kako, S. X. Ouyang, H. Stuart Williams, H. Yang, J. Y. Cao, W. J. Luo, Z. S. Li, Y. Liu, R. L. Withers, *Nat. Mater.* **2010**, *9*, 559.
[4] Z. G. Zou, J. H. Ye, K. Sayama, H. Arakawa, *Nature* **2001**, *414*, 625.
[5] S. Y. Reece, J. A. Hamel, K. Sung, T. D. Harvi, A. J. Esswein, J. J. H. Pijpers, D. G. Nocera, *Science* **2011**, *334*, 645.
[6] J. Zhang, J. G. Yu, Y. M. Zhang, Q. Li, J. R. Gong, *Nano Lett.* **2011**, *11*, 4774.
[7] S. Hoang, S. W. Guo, N. T. Hahn, A. J. Bard, C. B. Mullins, *Nano Lett.* **2012**, *12*, 26.
[8] K. Sivula, F. Le Formal, M. Gratzel, *ChemSusChem* **2011**, *4*, 432.
[9] I. S. Cho, Z. B. Chen, A. J. Forman, D. R. Kim, P. M. Rao, T. F. Jaramillo, X. L. Zheng, *Nano Lett.* **2011**, *11*, 4978.
[10] R. L. Bickley, G. C. Williams, *Mater. Chem. Phys.* **1997**, *51*, 47.
[11] Y. F. Sun, C. Z. Wu, R. Long, Y. Cui, S. D. Zhang, Y. Xie, *Chem. Commun.* **2009**, 4542.
[12] Y. F. Sun, Y. Xie, C. Z. Wu, S. D. Zhang, S. S. Jiang, *Nano Res.* **2010**, *3*, 620.
[13] S. W. Boettcher, J. M. Spurgeon, M. C. Putnam, E. L. Warren, D. B. Turner-Evans, M. D. Kelzenberg, J. R. Maiolo, H. A. Atwater, N. S. Lewis, *Science* **2010**, *327*, 185.
[14] H. J. Chang, E. J. In, K. J. Kong, J. O. Lee, Y. M. Choi, B. H. Ryu, *J. Phys. Chem. B* **2005**, *109*, 30.
[15] Y. C. Zhang, Z. N. Du, K. W. Li, M. Zhang, D. D. Dionysiou, *ACS Appl. Mater. Interfaces* **2011**, *3*, 1528.
[16] D. K. Ma, H. Y. Zhou, J. H. Zhang, Y. T. Qian, *Mater. Chem. Phys.* **2008**, *111*, 391.
[17] Y. C. Zhang, J. Li, M. Zhang, D. D. Dionysiou, *Environ. Sci. Technol.* **2011**, *45*, 9324.
[18] A. J. Smith, P. E. Meek, W. Y. Liang, *J. Phys. C* **1977**, *10*, 1321.
[19] H. S. S. Ramakrishna Matte, A. Gomathi, A. K. Manna, D. J. Late, R. J. Datta, S. K. Pati, C. N. R. Rao, *Angew. Chem.* **2011**, *122*, 4153; *Angew. Chem. Int. Ed.* **2011**, *50*, 4059.
[20] G. M. Wang, H. Y. Wang, Y. C. Ling, Y. C. Tang, X. Y. Yang, R. C. Fitzmorris, C. C. Wang, J. Z. Zhang, Y. Li, *Nano. Lett.* **2011**, *11*, 3026.
[21] V. Cristino, S. Caramori, R. Argazzi, L. Meda, G. L. Marra, C. A. Bignozzi, *Langmuir* **2011**, *27*, 7276.
[22] R. H. Gonçalves, B. H. R. Lima, E. R. Leite, *J. Am. Chem. Soc.* **2011**, *133*, 6012.
[23] N. T. Hahn, H. Ye, D. W. Flaherty, A. J. Bard, C. B. Mullins, *ACS Nano* **2010**, *4*, 1977.
[24] Y. H. Ng, A. Iwase, A. Kudo, R. Amal, *J. Phys. Chem. Lett.* **2010**, *1*, 2607.
[25] J. Z. Su, L. J. Guo, N. Z. Bao, C. A. Grimes, *Nano. Lett.* **2011**, *11*, 1928.
[26] J. C. Yu, X. C. Wang, X. Z. Fu, *Chem. Mater.* **2004**, *16*, 1523.
[27] J. W. Tang, Z. G. Zou, J. H. Ye, *Chem. Mater.* **2004**, *16*, 1644.
[28] Y. F. Sun, B. Y. Qu, S. S. Jiang, C. Z. Wu, B. C. Pan, Y. Xie, *Nanoscale* **2011**, *3*, 2609.
[29] F. Cardon, W. P. Gomes, *J. Phys. D* **1978**, *11*, L63.
[30] N. Takeda, B. A. Parkinson, *J. Am. Chem. Soc.* **2003**, *125*, 5559.
[31] G. M. Wang, Y. C. Ling, H. Y. Wang, X. Y. Yang, C. C. Wang, J. Z. Zhang, Y. Li, *Energy Environ. Sci.* **2012**, *5*, 6180.
[32] S. J. Hong, S. Lee, J. S. Jang, J. S. Lee, *Energy Environ. Sci.* **2011**, *4*, 1781.
[33] X. Y. Yang, A. Wolcott, G. M. Wang, A. Sobo, R. C. Fitzmorris, F. Qian, J. Z. Zhang, Y. Li, *Nano Lett.* **2009**, *9*, 2331.
[34] Q. Li, B. D. Guo, J. G. Yu, J. R. Ran, B. H. Zhang, H. J. Yan, J. R. Gong, *J. Am. Chem. Soc.* **2011**, *133*, 10878.
[35] M. Madl, W. Brezna, P. Klang, A. M. Andrews, G. Strasser, J. Smoliner, *Semicond. Sci. Technol.* **2010**, *25*, 065010.

